Journal of Petroleum Science and Engineering 219 (2022) 111076

Contents lists available at ScienceDirect

Journal of Petroleum Science and Engineering

journal homepage: www.elsevier.com/locate/petrol

Optimum sensor configuration of surface arrays for retrieving accurate source mechanisms of microseismic events

Yue Kong [a], Weimin Chen [b,c], Ning Liu [d], Boqi Kang [e], Min Li [a,*]

[a] School of Aeronautic Science and Engineering, Beihang University, Beijing, 100191, China
[b] Institute of Mechanics, Chinese Academy of Sciences, Beijing, 100190, China
[c] School of Engineering Science, University of Chinese Academy of Sciences, Beijing, 100049, China
[d] College of Mechanical and Electrical Engineering, Beijing University of Chemical Technology, Beijing, 100029, China
[e] Key Laboratory of Space Utilization, Technology and Engineering Center for Space Utilization, Chinese Academy of Sciences, Beijing, 100094, China

ARTICLE INFO

Keywords:
Moment tensor
Sensor configuration
Hydraulic fracturing
Optimization
Condition number

ABSTRACT

Hydraulic fracturing and induced networks are significant for effective production of oil and gas from unconventional resources. The knowledge of fracturing source mechanisms is helpful for optimizing hydraulic fracturing treatments to maximize production. For source monitoring, the moment tensor inversion is commonly used and the source mechanisms are interpreted by the radiation patterns of microseismic waves. The accuracy of source interpretation is significantly influenced by sensor configurations, which still need further researches. In this study, the mechanism of sensor arrangements to suppress noise effect is analyzed and clarified mathematically, then an optimization method of searching for proper sensor configurations is proposed. For superior sensor configurations, errors caused by noise can be allocated evenly to the 6 moment tensor components and the source interpretation based on the moment tensor decomposition is till accurate, but errors can not be completely eliminated by optimizing sensor configurations. Generally, high-precision inversion results can be calculated by the sensor configuration that one sensor is at the center and the others are around at the same angular intervals. Compared with tradition sensor configurations, this new one can achieve similar inversion accuracy by less than a third of the sensors. Sensor numbers are not the more the better and dependent on the sizes of the regions of sensor arrangement. The conclusions arrived in this study are helpful for evaluating and designing sensor configurations for hydraulic fracturing monitoring.

1. Introduction

In recent decades, the extraction of shale gas resources has been broadly developed to solve the energy issues. The exploration and commercial production for shale gas resources are carried out around the world (Li et al., 2019; Soeder, 2018). The shale oil and gas revolution has affected the global energy structure (Hughes, 2013). For adequate extraction of shale gas stored in the tight reservoirs, the key technology of hydraulic fracturing, which can initiate and extend fracture networks by high pressure fluid injection, is widely implemented to increase the permeability of resource reservoirs (Hossain et al., 2000; Zhuang and Zang, 2021). For the engineering applications of hydraulic fracturing, the knowledge of the source mechanisms of the cracks induced by hydraulic fracturing is extremely valuable for evaluating the performance of hydraulic fracturing treatments and optimizing the treatments for maximizing production and improving exploitation economics. Specifically, typical source mechanisms are in response to fluid injection and can be an indicator to show whether the hydraulic treatments work (Wu et al., 2019). In addition, source mechanisms are deeply related to the strain in the vicinity of fracturing sources and provide insights into the evolution of the stress field, which are helpful for predicting potential failure planes (Baig and Urbancic, 2010; Eyre and Van Der Baan, 2015). Moreover, the observation of source mechanisms is indispensable for the study of the principle of fracturing processes (Zhang et al., 2020). For retrieving source mechanisms, the moment tensor inversion is commonly used. Moment tensors represent the equivalent loads acting at the source and can be recovered by the radiation patterns of seismic waves induced by cracking (Aki and Richards, 2002). Then the fault plane parameters (strike, dip and rake of the fault) can be quantitatively computed by the decomposition of moment tensors (Kwiatek et al.,

* Corresponding author.
E-mail address: limin@buaa.edu.cn (M. Li).

https://doi.org/10.1016/j.petrol.2022.111076
Received 22 December 2021; Received in revised form 11 July 2022; Accepted 19 September 2022
Available online 23 September 2022
0920-4105/© 2022 Elsevier B.V. All rights reserved.

2014; Vavryčuk, 2015). The moment tensor inversion is an advanced method for quantitative source mechanism analysis and has been widely implemented in various engineering applications.

The moment tensor inversion is initially developed for seismic source monitoring. As early as 1964, Burridge and Knopoff (1964) firstly introduced the concept of the dynamic equivalence between body forces and seismic dislocations into the quantitative seismology analysis. Then Aki and Richards (2002) derived the complete formulas of the moment tensor theory and established the inversion framework based on the Green's function of unit concentrated moments. Based on the difference of signal processing, three inversion methods, which are the amplitude (Fojtíková et al., 2010; Godano et al., 2011; Vavryčuk et al., 2008), amplitude ratio (Hardebeck and Shearer, 2003; Jechumtálová and Šílený, 2005; Miller et al., 1998) and full waveform method (Dziewonski et al., 1981; Kikuchi and Kanamori, 1991; Šílený et al., 1992; Spikin, 1986), are used to invert for moment tensors. Among the three methods, the amplitude method can provide relatively accurate solutions in a simple way, thus is widely used in engineering applications. For extracting source mechanisms from retrieved moment tensors, the decompositions and source-type plot methods were also well explained (Hudson et al., 1989; Tape and Tape, 2012; Vavryčuk, 2015). At present, the moment tensor inversion is widely used for earthquake monitoring (Jian et al., 2018; Napoli and Ebel, 2018; Takemura et al., 2018; Vavryčuk et al., 2017). For microseismicity and acoustic emission (AE) events, the sources are essentially crack tip initiation and advance, which are the same as those of earthquakes. In addition, the energy release and moment tensor theory of earthquakes are also suitable for microseismicity and AE events. Consequently, the moment tensor inversion are being attempted in the two fields (Davi et al., 2013; Fischer and Guest, 2011; Jechumtalova and Eisner, 2008; Petruzalek et al., 2018; Wu et al., 2019; Xu et al., 2017).

For the moment tensor inversion, the inversion accuracy is significantly influenced by sensor configurations, because the waveforms recorded by sensors are always contaminated by noise (Dufumier and Rivera, 1997). Consequently, the sensor arrangement is a big issue for the engineering applications of the inversion. In the inversion for seismicity, the locations of seismic sources are unpredictable and the stations of recording seismic waves are always preset and permanent. Then the optimization of station positions is impossible and meaningless. However, in the inversion for microseismicity induced by hydraulic fracturing, the source locations are concentrated and predictable, because the sources are always close to the borehole. In addition, the sensor arrangement in the engineering applications of microseismicity monitoring is also optional. Thus, it is possible to optimize sensor configurations based on possible source locations to improve the inversion accuracy for moment tensors (Vavryčuk, 2007). In engineering applications, two sensor arrangements of borehole and surface arrays (Eyre and Van Der Baan, 2017) are commonly used. For borehole arrays, sensors are arranged underground, thus the effect of wave attenuation and inaccurate velocity models on inversion accuracy is relatively small, because the distances between sensors and sources are short (Jechumtalova and Eisner, 2008). But borehole arrays are always limited by specific engineering conditions and there are no general sensor configurations for different engineering applications. For surface arrays, sensors are all located on the surface and can achieve better focal coverage. The commonly-used configurations are the star shape of several arms with the same angular spacing and regular-grid shape over an area (Duncan and Eisner, 2010; Ren et al., 2020). Intrinsically, these two configurations tend to use a large amount of sensors to achieve relatively uniform coverage of the target area (Davi et al., 2013; Kwiatek et al., 2014; Ohtsu, 1991; Stierle et al., 2016; Yu et al., 2005), and are empirical and lack mathematical and physical basis. For evaluating and further improving the performance of traditional sensor configurations, some studies are carried out. Silený (2009) studied five configurations with different numbers of sensors, and the effect of event mislocations and inexact velocity models on the moment tensor inversion was well explained. Stanek et al. (2014) used the star-like and shallow borehole arrays to study the effect of noise and incorrect velocity models on the moment tensor inversion. Eyre and Van Der Baan (2017) compared the inversion accuracy between the surface and borehole arrays. The inversion results show that the surface array performs better than borehole arrays. Ren et al. (2020) studied the surface array of grid shapes and various shape parameters were considered in the research. The inversion results show that sensor numbers and some other configuration parameters should be carefully determined based on specific application conditions. In summary, those studies commonly used the enumeration method to investigate specific sensor configurations and the valuable conclusions were arrived by inversion simulations. In those studies, theoretical analysis is still insufficient and those conclusions only apply to specific sensor configurations. Consequently, the mechanism of sensor configurations to suppress the effect of noise needs to be well explained and a general method of determining sensor configurations is needed. In this paper, the inversion matrix is analyzed mathematically and the inversion accuracy of noisy conditions is explained by the matrix numerical calculation. Based on the above-mentioned analysis, an optimization method of selecting the positions of sensors is proposed, and the convergence and effectiveness of this method is validated by the synthetic tests. In addition, the sensor arrangements for some general conditions are studied by the new method and the guidelines of sensor configurations are arrived. These guidelines are helpful for the design and evaluation of sensor configurations.

2. Moment tensor theory

2.1. Inversion formulas

A microseismic source can be mathematically described by a moment tensor (Aki and Richards, 2002), the elements of which for isotropic media can be written as:

$$m_{pq} = \left(\lambda l_k v_k \delta_{pq} + \mu l_p v_q + \mu l_q v_p\right) s_{\mathrm{F}}, \tag{1}$$

where m_{pq} are the moment tensor elements, $p = 1, 2, 3$ and $q = 1, 2, 3$ represent X, Y, Z directions, λ and μ are the Lame constants, δ_{pq} is the Kronecher delta. l_k, l_p and l_q are the elements of the displacement vector of crack surfaces. v_k, v_p and v_q are the elements of the normal vector to crack surfaces, s_{F} is the crack size. According to Eq. (1), moment tensors are symmetrical and 6 of the 9 elements are independent of each other.

In terms of moment tensors, the far-field compressional waves (P waves) induced by a fracturing source can be expressed according to Aki and Richards (2002) as:

$$u^i(\mathbf{x}, t) = \frac{1}{4\pi\rho\alpha^3}\frac{r_i}{R_{\mathrm{S}}}\begin{pmatrix} r_1 & r_2 & r_3 \end{pmatrix}\begin{bmatrix} m_{11} & m_{12} & m_{13} \\ m_{12} & m_{22} & m_{23} \\ m_{13} & m_{23} & m_{33} \end{bmatrix}\begin{pmatrix} r_1 \\ r_2 \\ r_3 \end{pmatrix}\dot{S}(t), \tag{2}$$

where $u^i(\mathbf{x}, t)$ is the displacement in the ith direction ($i = 1, 2, 3$), r_1, r_2, r_3 are the direction cosine from sources to sensors, $\mathbf{x}$ is the location of a sensor and t is the time, ρ is the density of media and α is the P-wave velocity, R_{S} is the source-sensor distance and $S(t)$ is the source-time function, which describes the time-dependent opening state of crack surfaces. Actually, other waves can also be used for the moment tensor inversion and the following theoretical analysis is still suitable.

Based on the relationship of Eq. (2), moment tensors can be retrieved by recorded signals. For simplicity, source mechanisms are normally assumed to be independent of time history. Then the source-time function $S(t)$ is further assumed as a step function and the time derivation of $S(t)$ becomes an impulse function as follows (Liu et al., 2014):

$$\begin{cases} S(t) = \varepsilon(t) \\ \dot{S}(t) = \delta(t) \end{cases}, \tag{3}$$

where $\varepsilon(t)$ is a step function and $\delta(t)$ is an impulse function. Based on

Eqs. (2) and (3), the wave amplitude recorded by a sensor can be written as:

$$u^i = c\frac{r_i}{R_S}\begin{pmatrix} r_1 & r_2 & r_3 \end{pmatrix}\begin{bmatrix} m_{11} & m_{12} & m_{13} \\ m_{21} & m_{22} & m_{23} \\ m_{31} & m_{32} & m_{33} \end{bmatrix}\begin{pmatrix} r_1 \\ r_2 \\ r_3 \end{pmatrix}, \tag{4}$$

where u^i is the waveform amplitude, c is a coefficient and can be obtained by the pencil-lead break test in engineering applications. For a sensor array, according to Eq. (4), the wave amplitudes recorded by multiple sensors can be written as:

$$\begin{bmatrix} G_{11} & G_{12} & G_{13} & G_{14} & G_{15} & G_{16} \\ G_{21} & G_{22} & G_{23} & G_{24} & G_{25} & G_{26} \\ \vdots & \vdots & \vdots & \vdots & \vdots & \vdots \\ G_{n1} & G_{n2} & G_{n3} & G_{n4} & G_{n5} & G_{n6} \end{bmatrix}\begin{pmatrix} m_{11} \\ m_{12} \\ m_{13} \\ m_{22} \\ m_{23} \\ m_{33} \end{pmatrix} = \begin{pmatrix} u_1 \\ u_2 \\ \vdots \\ u_n \end{pmatrix}, \tag{5}$$

where G_{ij} ($i = 1, 2, \ldots, n; j = 1, 2 \ldots 6$) are the elements of the dynamic response matrix and dependent on relative positions between sources and sensors. Subscript n is the number of sensors. m_{pq} are the moment tensor elements to be solved. u_n are the amplitudes of waveforms and the superscript (in Eq. (4)) representing displacement directions is ignored for simplicity.

Intrinsically, the inversion for one source is to solve 6 unknown moment tensor elements, which means at least 6 equations ($n \geq 6$) in Eq. (5) are required for a source moment tensor inversion.

For simplicity, the matrix and vectors can be represented by letters and Eq. (5) can be rewritten as:

$$\mathbf{Gm} = \mathbf{u}, \tag{6}$$

where $\mathbf{G}$ is the dynamic response matrix, $\mathbf{m}$ is the vector of moment tensor elements, $\mathbf{u}$ is the vector of the amplitudes of waveforms. The solution of Eq. (6) can be calculated by the least-squares method (Sipkin, 1982):

$$\mathbf{m} = \left(\mathbf{G}^{\mathrm{T}}\mathbf{G}\right)^{-1}\mathbf{G}^{\mathrm{T}}\mathbf{u}. \tag{7}$$

For engineering applications, the waveforms recorded by sensors are always contaminated by noise, then the equation set of Eq. (6) becomes the following form:

$$\mathbf{G}(\mathbf{m} + \mathbf{m}_{\mathrm{E}}) = \mathbf{u} + \mathbf{u}_{\mathrm{N}}, \tag{8}$$

where $\mathbf{u}_{\mathrm{N}}$ is the vector of noise amplitudes, $\mathbf{m}_{\mathrm{E}}$ is the inversion errors caused by noise $\mathbf{u}_{\mathrm{N}}$. The relationship between $\mathbf{u}_{\mathrm{N}}$ and $\mathbf{m}_{\mathrm{E}}$ is dependent on sensor configurations and will be explained in Section 2.2.

2.2. Condition number

As stated in Section 2.1, the essence of the moment tensor inversion is to solve a set of linear equations. According to the numerical analysis theory (Xing and Cao, 2005), the solving accuracy of Eq. (6) is dependent on the condition number defined by Eq. (9).

$$\mathrm{cond}(\mathbf{G}) = \frac{\mathrm{maximum}(\mathrm{singular}-\mathrm{values}(\mathbf{G}))}{\mathrm{minimum}(\mathrm{singular}-\mathrm{values}(\mathbf{G}))}, \tag{9}$$

where the condition number cond($\mathbf{G}$) is defined as the ratio between the maximum and minimum singular values of the dynamic response matrix $\mathbf{G}$. For the moment tensor inversion, the physical mechanism and optimal value of the condition numbers can be explained by the singular value decomposition.

According to the singular value decomposition, the matrix $\mathbf{G}$ can be written as:

$$\mathbf{G} = \mathbf{ADB}^{\mathrm{H}} = \begin{bmatrix} \mathbf{A}_1 & \mathbf{A}_2 & \ldots & \mathbf{A}_6 \end{bmatrix}\begin{bmatrix} D_1 & 0 & \cdots & 0 \\ 0 & D_2 & & \vdots \\ \vdots & & \ddots & 0 \\ 0 & \cdots & 0 & D_6 \end{bmatrix}\begin{bmatrix} \mathbf{B}_1 & \mathbf{B}_2 & \cdots & \mathbf{B}_6 \end{bmatrix}^{\mathrm{H}}, \tag{10}$$

where matrices $\mathbf{A}$ and $\mathbf{B}$ are real orthogonal. $\mathbf{D}$ is a square diagonal matrix and its diagonal elements D_i ($i = 1, 2, \ldots, 6$) are the singular values of $\mathbf{G}$ in descending order. Then Eq. (6) can be written as:

$$\mathbf{ADB}^{\mathrm{H}}\mathbf{m} = \mathbf{u}, \tag{11}$$

where the vectors $\mathbf{m}$ and $\mathbf{u}$ can be expressed as the linear combinations of the column vectors of $\mathbf{A}$ and $\mathbf{B}$ respectively as:

$$\begin{cases} \mathbf{m} = \begin{bmatrix} \mathbf{B}_1 & \mathbf{B}_2 & \cdots & \mathbf{B}_6 \end{bmatrix}\begin{pmatrix} m_1 & m_2 & \cdots & m_6 \end{pmatrix}^{\mathrm{H}} \\ \mathbf{u} = \begin{bmatrix} \mathbf{A}_1 & \mathbf{A}_2 & \cdots & \mathbf{A}_6 \end{bmatrix}\begin{pmatrix} u_1^* & u_2^* & \cdots & u_6^* \end{pmatrix}^{\mathrm{H}} \end{cases}, \tag{12}$$

where m_i and u_i^* are the coordinates of the vectors $\mathbf{m}$ and $\mathbf{u}$ according to the basic vectors $\mathbf{A}_i$ and $\mathbf{B}_i$, which are the column vectors of the matrices $\mathbf{A}$ and $\mathbf{B}$. Then the following expression can be obtained:

$$\begin{bmatrix} D_1 & 0 & 0 & 0 & 0 & 0 \\ 0 & D_2 & 0 & 0 & 0 & 0 \\ 0 & 0 & D_3 & 0 & 0 & 0 \\ 0 & 0 & 0 & D_4 & 0 & 0 \\ 0 & 0 & 0 & 0 & D_5 & 0 \\ 0 & 0 & 0 & 0 & 0 & D_6 \end{bmatrix}\begin{pmatrix} m_1 \\ m_2 \\ m_3 \\ m_4 \\ m_5 \\ m_6 \end{pmatrix} = \begin{pmatrix} u_1^* \\ u_2^* \\ u_3^* \\ u_4^* \\ u_5^* \\ u_6^* \end{pmatrix}. \tag{13}$$

For the moment tensor inversion, unpredictable perturbations of wave amplitudes are induced by noise and inversion errors are generated. Then the equation set of Eq. (13) with noise involved can be written as follows:

$$\begin{bmatrix} D_1 & 0 & 0 & 0 & 0 & 0 \\ 0 & D_2 & 0 & 0 & 0 & 0 \\ 0 & 0 & D_3 & 0 & 0 & 0 \\ 0 & 0 & 0 & D_4 & 0 & 0 \\ 0 & 0 & 0 & 0 & D_5 & 0 \\ 0 & 0 & 0 & 0 & 0 & D_6 \end{bmatrix}\left(\begin{pmatrix} m_1 \\ m_2 \\ m_3 \\ m_4 \\ m_5 \\ m_6 \end{pmatrix} + \begin{pmatrix} m_1^{\mathrm{N}} \\ m_2^{\mathrm{N}} \\ m_3^{\mathrm{N}} \\ m_4^{\mathrm{N}} \\ m_5^{\mathrm{N}} \\ m_6^{\mathrm{N}} \end{pmatrix}\right) = \begin{pmatrix} u_1^* \\ u_2^* \\ u_3^* \\ u_4^* \\ u_5^* \\ u_6^* \end{pmatrix} + \begin{pmatrix} u_1^{\mathrm{N}} \\ u_2^{\mathrm{N}} \\ u_3^{\mathrm{N}} \\ u_4^{\mathrm{N}} \\ u_5^{\mathrm{N}} \\ u_6^{\mathrm{N}} \end{pmatrix}, \tag{14}$$

where m_i^{N} are the inversion errors caused by noise u_i^{N}. Based on Eq. (14), the relationship of Eq. (15) can be obtained.

$$m_1^{\mathrm{N}} = \frac{u_1^{\mathrm{N}}}{D_1}, m_2^{\mathrm{N}} = \frac{u_2^{\mathrm{N}}}{D_2}, \cdots, m_6^{\mathrm{N}} = \frac{u_6^{\mathrm{N}}}{D_6}. \tag{15}$$

In practical engineering applications, recorded waveforms are always contaminated by noise induced by various factors and the noise u_i^{N} can hardly be predicted precisely. For simplicity, it is assumed that the noise recorded by different sensors is independent of each other and the noise amplitudes satisfy the relationship of $u_1^{\mathrm{N}} = u_2^{\mathrm{N}} = \ldots = u_6^{\mathrm{N}}$. The effectiveness of the assumptions can be validated by the synthetic tests in Section 4. Then the optimal value of the condition numbers can be further derived.

For the interpretation of source mechanisms, the retrieved moment tensors are commonly decomposed into three basic tensors and the source mechanisms are identified by the proportions of the tensors (Vavryčuk, 2015). Obviously, the interpretation accuracy are dependent on the relative magnitude between moment tensor elements. For improving the inversion accuracy of noisy conditions, the relationship of Eq. (16) should be satisfied as far as possible.

$$\left(m_1+m_1^{\mathrm{N}}\right):\left(m_2+m_2^{\mathrm{N}}\right):\cdots:\left(m_6+m_6^{\mathrm{N}}\right)=m_1:m_2:\cdots:m_6. \tag{16}$$

However, source mechanisms are unknown before the inversion, which means the real relative magnitude between moment tensor elements is uncertain. Because the errors m_i^{N} are commonly much smaller than the solutions m_i, for generality, we can make the formula of Eq. (17) as strong as possible.

$$m_1^{\mathrm{N}}=m_2^{\mathrm{N}}=\cdots=m_6^{\mathrm{N}}. \tag{17}$$

Based on Eqs. (15) and (17), for suppressing the effect of noise, it can be concluded that the relation of Eq. (18) should be satisfied.

$$D_1=D_2=\cdots=D_6. \tag{18}$$

It should be noted that the relationship of Eq. (18) is the simplification of Eq. (16) and the satisfaction of Eq. (18) cannot make Eq. (16) set up completely. Thus, the satisfaction of Eq. (18) can not eliminate errors completely. However, because the real moment tensor is unknown before the inversion, Eq. (18) is more suitable for general engineering applications than Eq. (16). For improving inversion accuracy, we can only make D_1 as close to D_6 as possible, which means the condition number defined as D_1/D_6 should be close to 1. Actually, for engineering applications, a perfect sensor configuration is nonexistent to make Eq. (18) set up strictly and the condition number of 1 can hardly be achieved. Consequently, it can be concluded that the smaller the condition number is, the better the performance of the sensor configuration.

The mechanisms of sensor configuration optimization can also be explained in some plain languages. The singular values describe the actions of the moments (moment tensor elements) to waveforms and the condition number represents the relative magnitude between the maximum and minimum actions. A small condition number indicates that the errors can be evenly allocated to all the solved moment tensor elements. If the condition number is too large, the errors of some solved moment tensor elements will be far greater than those of the other elements, then the relative magnitude between solved moment tensor elements changes dramatically and the decomposition of the moment tensors will provide inaccurate source-type interpretation. Proper sensor configurations with relatively small condition numbers can coordinate the actions of moment tensor elements. Moreover, the information recorded by 6 sensors is sufficient to invert for the moment tensor of a source, but the ratio between the maximum and minimum actions may not be good enough to suppress the effect of noise. Consequently, extra sensors are needed for the inversion to reduce the condition numbers, then unpredictable errors are more evenly distributed to all solved moment tensor elements and the accuracy of source-type interpretation improves.

It should be noted that the assumption of $u_1^{\mathrm{N}}=u_2^{\mathrm{N}}=\ldots=u_6^{\mathrm{N}}$ in Eqs. (15)-(16) is conservative for noise distribution. There are more serious cases of noise distribution for the moment tensor inversion. However, for other ratios of $u_1^{\mathrm{N}}=u_2^{\mathrm{N}}=\ldots=u_6^{\mathrm{N}}$, the optimal condition number will be larger than 1 and quite different for different cases according to Eqs.(16)-(18). Then no general conclusions can be obtained. Moreover, for theoretical analysis, the enumeration method for the ratios of 6 values are quite complex and difficult. For engineering applications, the real ratios of $u_1^{\mathrm{N}}=u_2^{\mathrm{N}}=\ldots=u_6^{\mathrm{N}}$ can hardly be identified before the inversion. Consequently, the assumption of $u_1^{\mathrm{N}}=u_2^{\mathrm{N}}=\ldots=u_6^{\mathrm{N}}$ is the most practical one.

3. Optimization method of sensor configuration

For engineering applications, the conditions for the moment tensor inversion vary greatly and a general method of searching for proper sensor configurations is needed.

According to the theoretical analysis in Section 2, the condition number is the indicator of the performance of sensor configurations. Consequently, sensor configurations can be optimized by the principle of the condition numbers. This optimization problem of sensor arrangements can be written as Eq. (19).

$$\begin{cases}\min\{\mathrm{cond}(\mathbf{G}(\mathbf{x})\}\\ \mathrm{F}(\mathbf{x})\le 0\end{cases}, \tag{19}$$

where the condition number cond(G(**x**)) is the objective function and the target value of 1 is wanted. F(**x**)≤0 is the constraint function, which describes that the sensors should be deployed in specific regions and their coordinates should satisfy specific conditions. **x** is the positions of sensors as follows:

$$\mathbf{x}=\begin{bmatrix}x_{11} & x_{12} & x_{13}\\ x_{21} & x_{22} & x_{23}\\ \vdots & \vdots & \vdots\\ x_{n1} & x_{n2} & x_{n3}\end{bmatrix}. \tag{20}$$

where x_{ij} ($i=1, 2, \ldots,\mathrm{n}; j=1, 2, 3$) is the jth coordinate of the ith sensor. The common iterative form of solving optimization problems can be written as:

$$\mathbf{x}^{k+1}=\mathbf{x}^k+\beta\Delta\mathbf{x}^k, \tag{21}$$

where $\mathbf{x}^{k+1}$ and $\mathbf{x}^k$ are the optimization solutions at the k+1 and k iterations. β is the step size, which defines the distance of each iteration. $\triangle\mathbf{x}^k$ is the iterative direction of the kth step. For the moment tensor inversion, condition numbers are expressed in terms of the coordinates of sensors and have poor differential properties. Consequently, the analytical methods of determining iterative directions, such as steep descent direction method (Savard and Gauvin, 1994), the Newton's method (Battiti, 1992) and quasi-Newton based method (Loke and Barker, 1996), are not suitable for this problem.

In this study, we proposed an iteration approach based on the optimization method of random directions. Unlike the traditional approach, in which the sampling directions are randomly generated, the sampling directions for the new iteration approach is defined as Eq. (22). In Eq. (22), the sampling directions are defined by the coordinate component of all sensors. According to the theoretical analysis, condition numbers are always seriously affected by particular coordinates of specific sensors and the sampling directions of Eq. (22) are helpful for improving the iteration efficiency. Change of one coordinate component of one sensor is one sampling direction, which is actually a sampling group of sensor positions. Then n sensors with $3\times n$ coordinate components require $6\times n$ sampling groups at each iteration step. The sampling sensor group $\mathbf{x}+\beta\triangle\mathbf{x}$ (sensor configuration) with the minimum condition number is the solution in this iteration step.

$$\Delta\mathbf{x}_1 = \begin{bmatrix} 1 & 0 & 0 \\ 0 & 0 & 0 \\ \vdots & \vdots & \vdots \\ 0 & 0 & 0 \end{bmatrix}, \Delta\mathbf{x}_2 = \begin{bmatrix} -1 & 0 & 0 \\ 0 & 0 & 0 \\ \vdots & \vdots & \vdots \\ 0 & 0 & 0 \end{bmatrix},$$

$$\Delta\mathbf{x}_3 = \begin{bmatrix} 0 & 1 & 0 \\ 0 & 0 & 0 \\ \vdots & \vdots & \vdots \\ 0 & 0 & 0 \end{bmatrix}, \Delta\mathbf{x}_4 = \begin{bmatrix} 0 & -1 & 0 \\ 0 & 0 & 0 \\ \vdots & \vdots & \vdots \\ 0 & 0 & 0 \end{bmatrix},$$

$$\Delta\mathbf{x}_5 = \begin{bmatrix} 0 & 0 & 1 \\ 0 & 0 & 0 \\ \vdots & \vdots & \vdots \\ 0 & 0 & 0 \end{bmatrix}, \Delta\mathbf{x}_6 = \begin{bmatrix} 0 & 0 & -1 \\ 0 & 0 & 0 \\ \vdots & \vdots & \vdots \\ 0 & 0 & 0 \end{bmatrix}, \quad (22)$$

$$\vdots$$

$$\Delta\mathbf{x}_{6n-1} = \begin{bmatrix} 0 & 0 & 0 \\ 0 & 0 & 0 \\ \vdots & \vdots & \vdots \\ 0 & 0 & 1 \end{bmatrix}, \Delta\mathbf{x}_{6n} \begin{bmatrix} 0 & 0 & 0 \\ 0 & 0 & 0 \\ \vdots & \vdots & \vdots \\ 0 & 0 & -1 \end{bmatrix}.$$

According to the theoretical analysis above, an optimization approach can be summarized as follows:

(1) Set initial parameters and stopping criterions.

The initial parameters are approximate source locations, initial guesses of sensor positions and initial step sizes. (a) Approximate source locations can be estimated by the locations of the horizontal wells in hydraulic fracturing stages and the errors caused by the source deviations from real to estimated locations are relatively small, which will be proved in Section 5.3. (b) The initial guesses of sensor positions are randomly selected in the feasible region, in which sensors can be deployed. (c) Initial step sizes are not fixed, but should be relatively large to sufficiently explore all the solution space.

Two stopping criterions of the thresholds of step sizes and condition numbers are used for the optimization iteration. When either of the two thresholds is satisfied, the iteration stops.

After the above setup is complete, step 2 is executed.

(2) Calculate the sensor positions of sampling groups.

The sensor positions of sampling groups are calculated by $\mathbf{x}_j = \mathrm{x}^{k-1} + \beta\triangle\mathbf{x}_j$ (j = 1, 2, …,6n). $\mathbf{x}_j$ are the sensor positions of sampling groups. x^{k-1} is the solution of the last iteration step. β are step sizes. $\triangle\mathbf{x}_j$ are the sampling directions and calculated by Eq. (22). Then 6n sampling sensor groups are obtained in each iteration step. If some sensor positions are outside feasible regions, those positions can be replaced by the ones in the last iteration step, then step 3 is executed. If the sensor positions of all sampling groups are outside feasible regions, step 5 is executed.

(3) Calculate condition numbers.

The condition numbers of all sampling sensor groups are calculated by Eq. (9). 6n condition numbers can be obtained in each iteration step, then step 4 is executed.

(4) Pick the sensor group of the minimum condition number.

Among the 6n condition numbers, the minimum one and the corresponding sensor group are picked. If the condition number is larger than that in the last iteration step, step 5 is executed. If not, step 6 is executed.

(5) Reduce step sizes.

Step sizes are recommended to be reduced by a constant ratio. If the new step size is smaller than the threshold, the iteration stops and step 7 is executed. If not, step 2 is executed and a new iteration loop is carried out.

(6) Update new sensor configuration.

The new sensor configuration is obtained. If the condition number of the new sensor configuration is larger than the threshold, step 2 is executed and the new sensor configuration is set as the initial solution for the next iteration loop. If not, step 7 is executed.

(7) The best sensor configuration is obtained.

The flow chart of the algorithm is plotted in Fig. 1.

4. Sensor configuration in a circular region

For evaluating the optimization method of searching for sensor arrangements, synthetic tests are carried out in this section. For the synthetic tests, true source mechanisms are known before the inversion and the inversion accuracy can be measured quantitatively. In addition, a large number of sensor configurations can be tested efficiently. Moreover, appropriate experimental equipment or seismic data are not available for us, thus the synthetic tests are carried out.

For the reliability of the synthetic tests, the synthetic seismic data are calculated by the Green's function (Aki and Richards, 2002) and a representative source-time function, which is expressed according to Ohtsu (1988) as:

$$S(t) = \begin{cases} \dfrac{t}{T_\mathrm{R}} - \dfrac{2}{3\pi}\sin\left(\dfrac{2\pi t}{T_\mathrm{R}}\right) + \dfrac{1}{12\pi}\sin\left(\dfrac{4\pi t}{T_\mathrm{R}}\right) & t < T_\mathrm{R} \\ 1 & t \geq T_\mathrm{R} \end{cases} \quad (23)$$

where $S(t)$ is the source-time function, t is the time and T_R is the rise

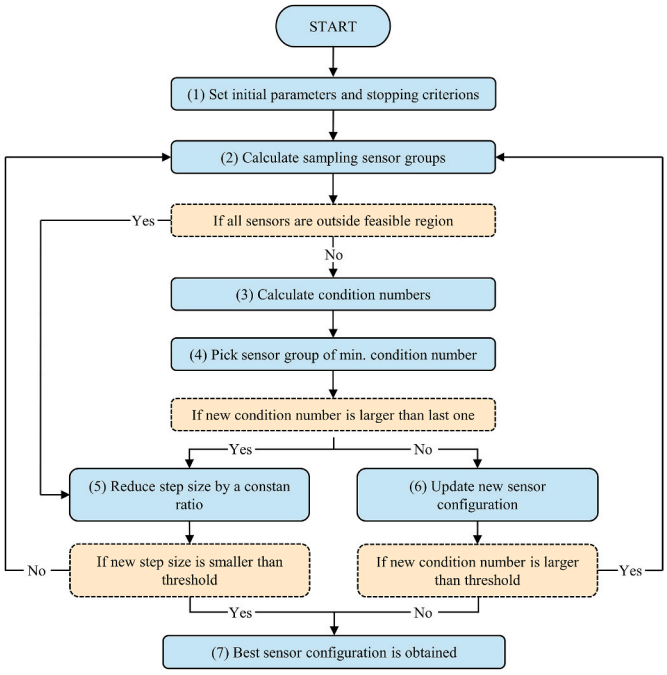

Fig. 1. Flow chart of the algorithm of the optimization method. The frames of solid lines represent execution steps and the frames of dotted lines represent judgment steps.

time. The waveforms calculated by Eq. (23) are in good agreements with the recorded signals (Ohtsu, 1988).

For achieving a good coverage over the focal sphere, we studied the surface arrays. Here we assume that sensors can be deployed in a circular surface region. The sensor configurations are optimized by the method proposed in Section 3. Circulars are the simplest shape, by which some general conclusions for sensor arrangements can be arrived.

The relative positions between the feasible region and approximate sources are plotted in Fig. 2. The feasible region, in which sensors can be deployed, is the circular with a radius of R on the surface. We assumed homogeneous and isotropic media as Ren et al. (2020) did and the uncertainties in the inversion are represented by random white noise for simplicity.

Referring to some model data (Eyre and Van Der Baan, 2017; Jechumtalova and Eisner, 2008), the parameters are set as follows: the depth H of the source is 1000 m and the radius R of the region is 500 m. The initial guesses of sensor configurations are randomly selected in the circular region. The material parameters are listed in Table 1. For simplicity, wave attenuation and heterogeneity are ignored in the model, because the influence of those two factors on inversion accuracy is dependent on the accuracy of velocity models and not related to sensor configurations. Displacements perpendicular to the surface are used to invert for moment tensors.

For the optimization processes, the initial guesses of sensor positions are randomly selected in the feasible region, in which sensors can be deployed. The initial step size is $R/10$ and the step size reduces by half for each step size reduction. The threshold of step sizes is 1/1000 of the initial step size. The estimated source locations are selected as the true coordinates and the effect of the source deviations from real to estimated locations will be discussed in Section 5.3. The threshold of condition numbers is 1.

In practical engineering applications, the waveforms recorded by sensors are affected by many complex factors, such as temperature, pressure, moisture, etc. Those factors may introduce noise into recorded waveforms, then the inversion accuracy for moment tensors is reduced. However, the effect of those factors can hardly be identified. For generality and simplicity, no specific complex factors are commonly involved and the effect of those complex factors is generally represented by random white noise (Eyre and Van Der Baan, 2017; Stierle et al., 2016; Vavryčuk et al., 2017). The synthetic tests in this study are also intended for some general cases and the random white noise with a uniform distribution is used in the synthetic tests. Obviously, for a specific practical engineering application, the noise introduced by complex factors may not be randomly distributed. The inversion solutions of random white noise may be different from those of real noise, but the conclusions are still effective for engineering applications.

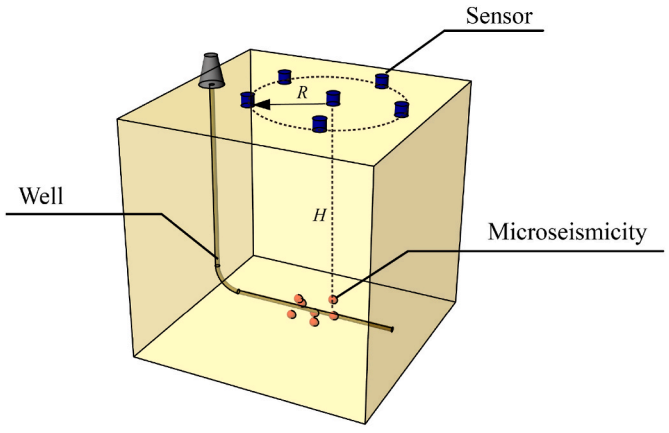

Fig. 2. Relative positions between the sources and feasible region. The feasible region is for sensors being deployed in and has a circular shape with the radius of R.

Table 1
Material parameters.

Parameter	Elastic module	Poisson ratio	Density	P-wave velocity
Value	5.4×10^{10}Pa	0.25	3200 kg/m^3	4500 m/s

The seismometers of seismic stations are commonly used for the hydraulic fracturing monitoring under natural conditions (Yu et al., 2018) and wideband or resonant piezoelectric sensors (acoustic emission sensors) are commonly used for the laboratory-scale experiments of hydraulic fracturing (Hampton et al., 2019; Wu et al., 2019). Commonly-used seismometers convert elastic waves to electric signals by the electromagnetic induction (Shearer, 2009) and piezoelectric sensors are based on the piezoelectric effect (Grosse and Ohtsu, 2008). Each seismometer or piezoelectric sensor has specific parameters (such as the frequency range and resonance of piezoelectric sensors etc.) and the performance of recording signals is dependent on various factors, such as sensor sensitivity, installation, calibration etc. (Davi et al., 2013). For simplicity and generality, no specific sensor types are involved in the synthetic tests and the possible errors caused by sensors are represented by random white noise.

4.1. Optimized sensor configuration

For the synthetic tests, one-channel sensors are used for the moment tensor inversion. One amplitude of a waveform can be obtained by one sensor and 6 unknown elements of a moment tensor require at least 6 amplitudes for the inversion of one source. Consequently, 6 sensors are the minimum number required for a source moment tensor inversion and we studied the configuration of 6 sensors firstly. By the optimization method, the final configurations of 6 sensors optimized by three randomly-selected initial guesses are obtained and plotted in Fig. 3.

For the 3 optimization processes in Fig. 3, the condition numbers change with iteration numbers and the relations are plotted in Fig. 4.

As shown in Fig. 3, the 3 optimized sensor configurations are similar that 1 sensor locates at the center and the other 5 locate around. Because the feasible region is circular and centrosymmetric, the 3 solutions in Fig. 3 are actually the same, which can be verified by Fig. 4. As shown in Fig. 4, the initial condition numbers are different for the three optimization processes, which indicates that the randomly-selected initial guesses are different. After the optimization processes, the three final optimized sensor configurations have the same condition number, thus the 3 configurations are actually the same. This configuration obtained by the optimization method is also the same as that obtained by the Monte Carlo strategy (Kong et al., 2019). According to the results above, the efficiency and convergence of the optimization method for 6 sensors is confirmed.

We also studied the sensor configurations of more than 6 sensors using the optimization method. The optimization solutions for 9, 12 and 15 sensors are plotted in Fig. 5. The initial guesses are randomly selected by the program.

As shown in Fig. 5, for 9 sensors, the optimized configuration is that 4 sensors are located at the center of the feasible region and the other 5 locate around. For 12 sensors, the optimized configuration is that 5 sensors locate at the center and the other 7 locate around. Similar characteristics can be observed for 15 sensors that 6 sensors locate at the center and 9 sensors locate around. This sensor configuration is different from traditional ones and can be called the center-boundary one.

Based on the optimization solutions above, an unusual phenomenon for sensor configurations can be observed that multiple sensors are deployed in the same position and the others locate around. This phenomenon is a bit strange and will be explained in Section 4.2.

4.2. Explanation of optimization results

According to the optimization results of sensor configurations, the

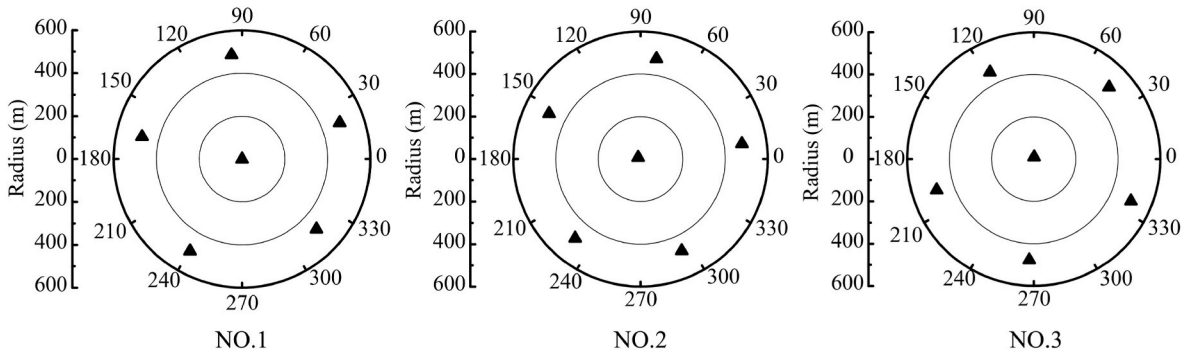

Fig. 3. 3 final optimization solutions of sensor configurations for 6 sensors. The triangle symbols represent the sensors. The initial guesses of sensor configurations are randomly selected by the program. The feasible region, in which sensors can be deployed, is circular and the radius is 500 m.

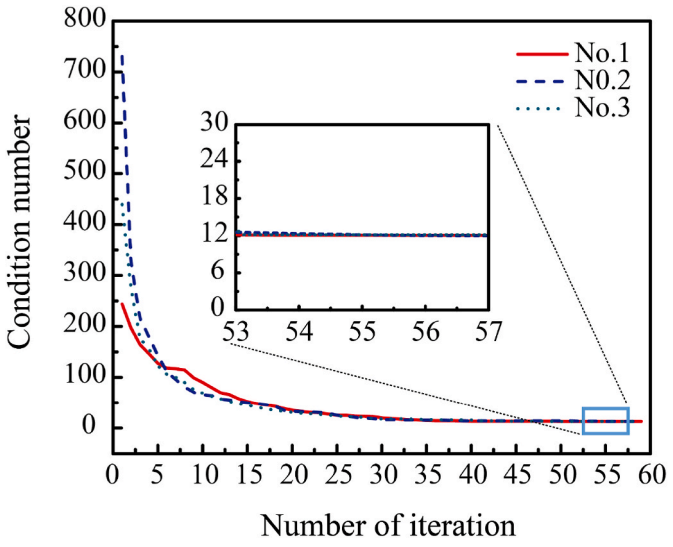

Fig. 4. Condition numbers for different iteration numbers during the 3 optimization processes of Fig. 3.

best inversion accuracy can be achieved by the configurations with multiple sensors arranged in the same place and this result is uncommon. In this section, the phenomenon of multiple sensors arranged in one place is explained.

Multiple sensors arranged in the same place is uncommon for engineering applications and this result is caused by the independence assumption. In the theoretical analysis of Section 2.2, it is assumed that the noise recorded by different sensors is independent of each other. Actually, the information recorded by 6 sensors are adequate to invert for a source. More sensors arranged in the same place are helpful for improving inversion accuracy, if the noise recorded by different sensors is independent of each other.

For path dependent noise, multiple sensors arranged in the same place is useless for improving inversion accuracy. If noise is related to wave propagation paths, noise recorded by different sensors in the same place is the same and the noise can not cancel each other, which can be proved by the inversion matrix. If f of n sensors are in the same place, the inversion matrix can be written as Eq. (24). n is the total sensor number. Obviously, f sensors in the same place result in f identical rows in the inversion matrix.

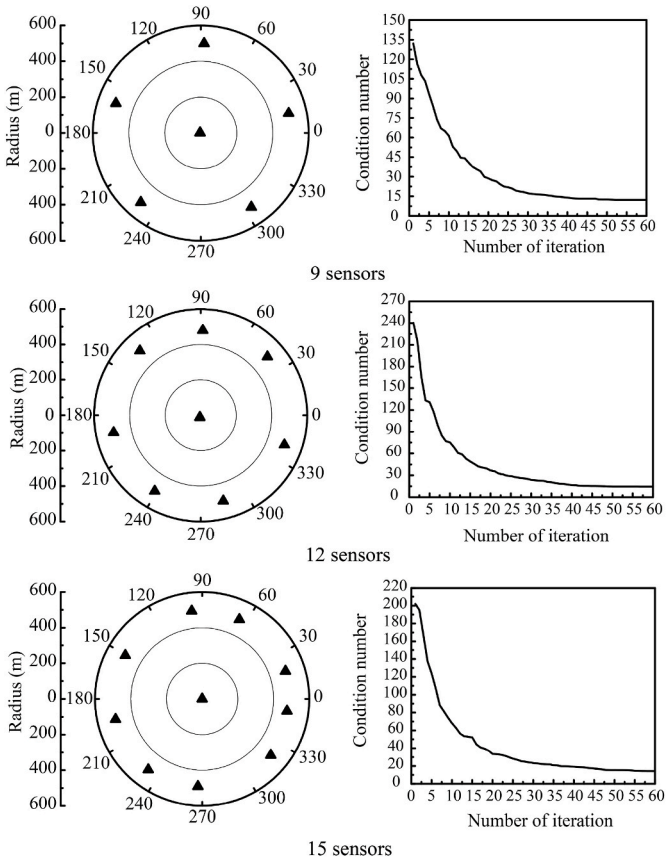

Fig. 5. Optimization solutions of sensor configurations for 9, 12 and 15 sensors, and the condition numbers for the iteration numbers. The triangle symbols represent the sensors.

$$\begin{bmatrix} G_{11} & G_{12} & G_{13} & G_{14} & G_{15} & G_{16} \\ G_{21} & G_{22} & G_{23} & G_{24} & G_{25} & G_{26} \\ \vdots & \vdots & \vdots & \vdots & \vdots & \vdots \\ G^1_{k1} & G^1_{k2} & G^1_{k3} & G^1_{k4} & G^1_{k5} & G^1_{k6} \\ \vdots & \vdots & \vdots & \vdots & \vdots & \vdots \\ G^f_{k1} & G^f_{k2} & G^f_{k3} & G^f_{k4} & G^f_{k5} & G^f_{k6} \\ \vdots & \vdots & \vdots & \vdots & \vdots & \vdots \\ G_{n1} & G_{n1} & G_{n1} & G_{n1} & G_{n1} & G_{n1} \end{bmatrix} \begin{pmatrix} m_{11} \\ m_{12} \\ m_{13} \\ m_{22} \\ m_{23} \\ m_{33} \end{pmatrix} = \begin{pmatrix} u_1 \\ u_2 \\ \vdots \\ u^1_k \\ \vdots \\ u^f_k \\ \vdots \\ u_n \end{pmatrix}, \tag{24}$$

where $G^1_{ki} = G^f_{ki}$ $(i = 1, 2, \ldots, 6)$ and $u^1_k = u^f_k$.

If we reduce the sensor number and put only one sensor in that place, the inversion matrix changes from Eq. (24) to Eq. (25).

$$\begin{bmatrix} G_{11} & G_{12} & G_{13} & G_{14} & G_{15} & G_{14} \\ G_{21} & G_{22} & G_{23} & G_{24} & G_{25} & G_{26} \\ \vdots & \vdots & \vdots & \vdots & \vdots & \vdots \\ G^1_{k1} & G^1_{k2} & G^1_{k3} & G^1_{k4} & G^1_{k5} & G^1_{k6} \\ \vdots & \vdots & \vdots & \vdots & \vdots & \vdots \\ G_{w1} & G_{w2} & G_{w3} & G_{w4} & G_{w5} & G_{w6} \end{bmatrix} \begin{pmatrix} m_{11} \\ m_{12} \\ m_{13} \\ m_{22} \\ m_{23} \\ m_{33} \end{pmatrix} = \begin{pmatrix} u_1 \\ u_2 \\ \vdots \\ u^1_k \\ \vdots \\ u_w \end{pmatrix}, \tag{25}$$

where $w = n\text{-}f\text{+}1$. Obviously, the solution of Eq. (25) is the same as that of Eq. (24). Arranging multiple sensors in the same place is not helpful for improving inversion accuracy, if noise is dependent on wave propagation paths.

In summary, if noise recorded by different sensors is independent of each other, multiple sensors in one place can improve the inversion accuracy. If noise is dependent on wave propagation paths, multiple sensors in one place are not helpful for improving inversion accuracy and one sensor at the center is adequate. Even so, the center-boundary sensor configuration with one sensor at the center still has the advantage of inversion accuracy over traditional ones, which can be proved in Section 4.3.

4.3. Synthetic results

In this section, the synthetic tests of the moment tensor inversion are carried out to evaluate the performance of the optimized sensor configurations in Section 4.1. The synthetic seismic data are calculated by the Green's function (Vavryčuk, 2011) and the sources are pure tensile, which are commonly observed in hydraulic fracturing processes (Baig and Urbancic, 2010). The normal vector to the fault and the displacement vector of the fault are along the depth direction with the dip of 0° and slope of 90°. According to Eq. (13), the condition number is independent on source types, thus the performance of sensor configurations are not related to source types. Using one source type in the synthetic tests is efficient for the study.

We added random white noise into the seismic data to test the performance of sensor configurations. Random white noise is relatively representative and usually used for theoretical analysis and academic researches (Eyre and Van Der Baan, 2017; Vavryčuk et al., 2017). The noise levels are defined as the ratio R_N between the amplitudes of noise and those of signals. The ratios used in the synthetic tests are 10%, 20% and 30%. The amplitude inversion method is used to invert for moment tensors in this study.

For interpreting source mechanisms, the decomposition of moment tensors into the isotropic (ISO), double-couple (DC) and compensated linear vector dipole (CLVD) components is used (Vavryčuk, 2015). The proportions of DC components are commonly regarded as the indicator of inversion accuracy (Ren et al., 2020), because it is sensitive to various source types. The proportion of DC component for the moment tensor of a pure tensile dislocation is 0, which also benefits the comparison between the inversion results and true values.

For the moment tensor inversion of 6 sensors, the proportions of DC components of the moment tensor solutions are plotted in Fig. 6. During the optimization process, the optimized sensor configurations at specific iterations are picked out. For each sensor configuration and noise level, the inversion is repeated by 100 times and 100 DC proportions can be obtained. In Fig. 6, the numbers of iterations are plotted on the horizontal axis and the average of the 100 DC proportions are given by the ordinates. Error bars represent the standard deviations of the 100 DC proportions.

Fig. 6 suggests that the optimization iterations improve the performance of sensor configurations. For each noise level, as the iteration proceeds, the averaged DC proportions and standard deviations decrease, which means the performance of sensor configurations to suppress the effect of noise improves. The true DC proportion for a pure tensile dislocation is 0 and obviously the standard deviation is also 0, while no noise is added into the seismic data. In other words, the inversion accuracy improves as the iteration proceeds and the optimization is effective to improve the performance of sensor configurations.

For the moment tensor inversion of more than 6 sensors, the optimization is still effective. For the inversion of 9, 12 and 15 sensors, the averaged DC proportions and standard deviations of the retrieved moment tensors are plotted in Fig. 7.

Fig. 7 shows that, for the inversion of more sensors, the optimization process can improve the performance of sensor configurations. As the optimization proceeds, the inversion errors decrease and the solutions become stable, which is similar to those in the inversion of 6 sensors.

In summary, the optimization process is effective and it can be concluded that, for different numbers of sensors, the optimized sensor configurations have the same characteristic, which one sensor locates at

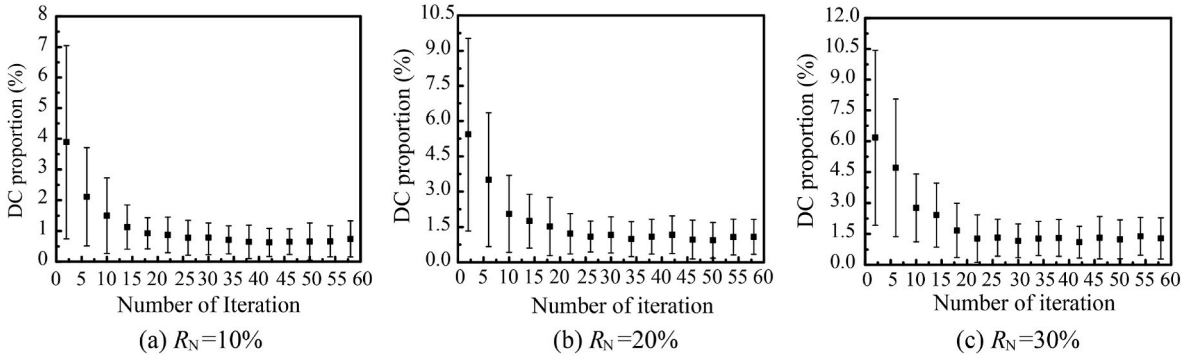

Fig. 6. For the moment tensor inversion of 6 sensors, the inversion errors for the sensor configurations at different iteration steps. The inversion errors are the averaged DC proportions of 100 repeated results and the true value is 0. Error bars are the standard deviations of the 100 DC proportions. Three noise levels, R_N = 10%, 20% and 30%, are involved.

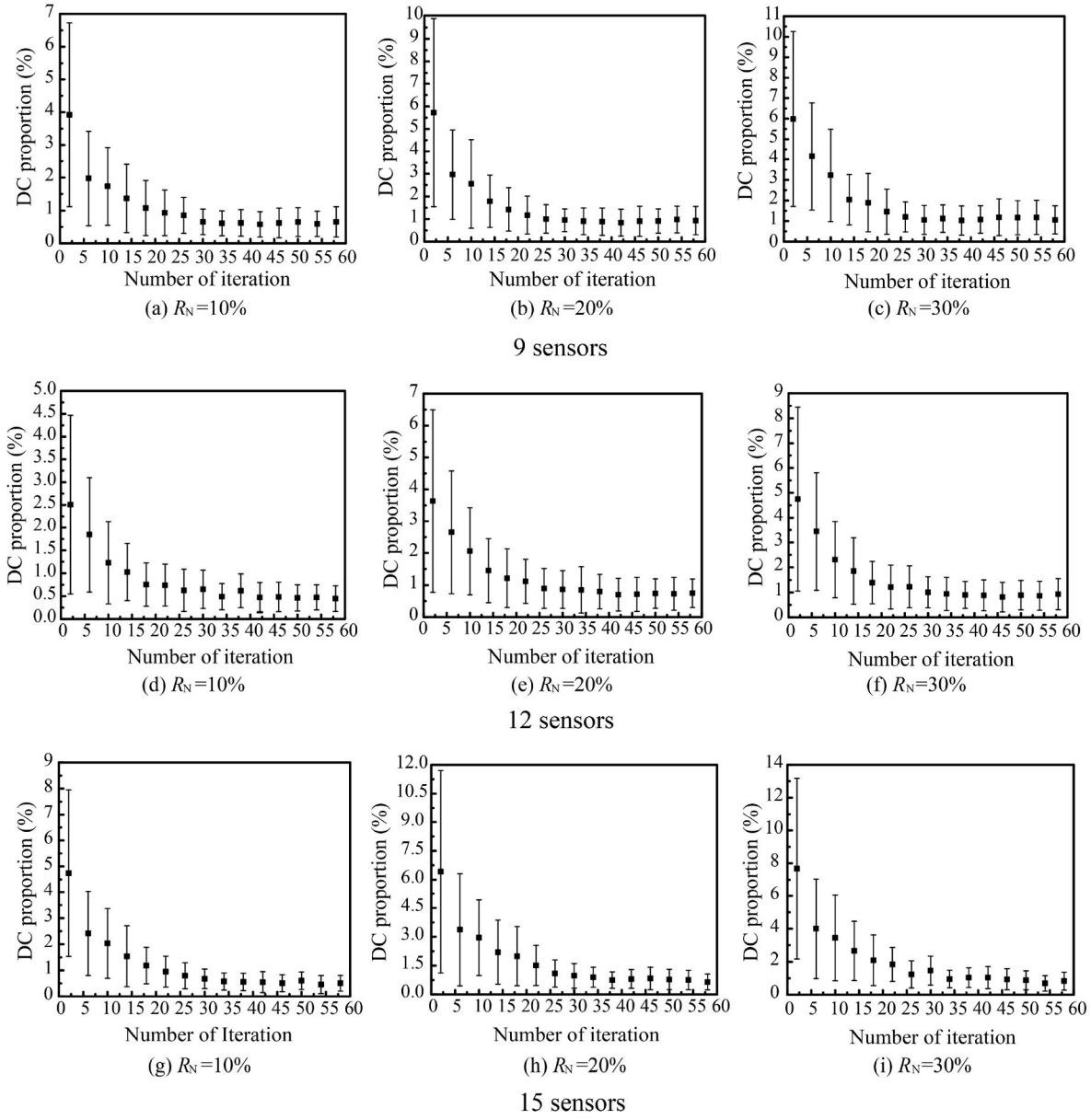

Fig. 7. For the inversion of 9, 12 and 15 sensors, the inversion errors for the sensor configurations at different iteration steps. Three noise levels, R_N = 10%, 20% and 30%, are involved.

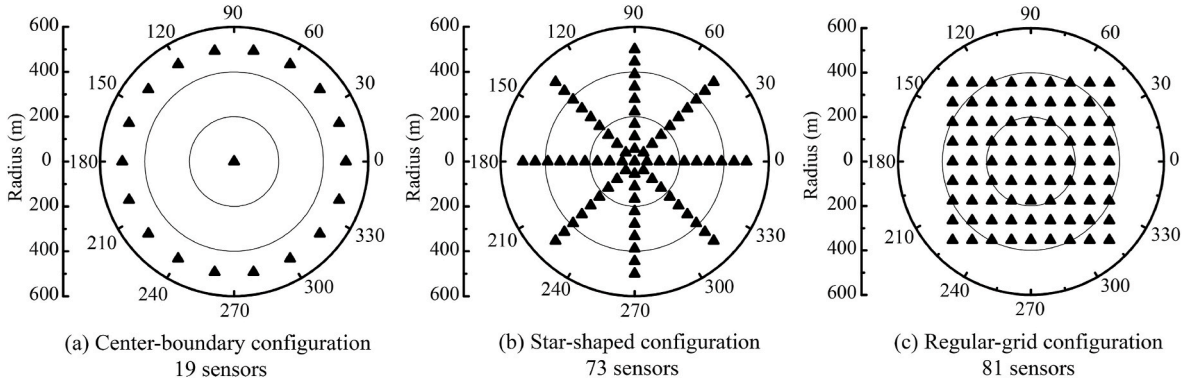

Fig. 8. Three sensor configurations: (a) the center-boundary one of 19 sensors (b) the star-shaped one of 73 sensors; (c) the regular-grid one of 81 sensors.

the center of the region and the others locate on the boundary of the region with the same azimuthal intervals. This new configuration is obviously different from the commonly-used ones and can be called the center-boundary configuration.

Compared with commonly-used sensor configurations, the center-boundary one has the advantage of inversion accuracy. We compared the inversion accuracy between the center-boundary and two commonly-used sensor configurations. The two commonly-used sensor configurations are star-shaped and regular-gird ones. According to Eyre and Van Der Baan (2017), the star-shaped configuration is arranged as Fig. 8(b) and 73 sensors are contained. The regular-grid configuration (Fig. 8(c)) contains 81 sensors of a 9 × 9 array. By contrast, as shown in Fig. 8(a), the center-boundary configuration contains 19 sensors, which one sensor locates at the center and the other 18 locate around.

The data of seismic waves is calculated by the Green's function. The inversion results of the three sensor configurations are plotted in Fig. 9. Because of different shapes of sensor configurations, it is difficult to keep the three sensor configurations containing same number of sensors. Consequently, we study the sensor numbers of different configurations under the same inversion accuracy.

As shown in Fig. 9, the errors increase with the increase of noise levels, but the inversion accuracy of the three sensor configurations are very close at every noise level. It should be noted that the numbers of sensors contained in the three configurations are 19, 72 and 81. In other words, the center-boundary configuration can achieve similar inversion accuracy by quarter number of sensors of the star-shaped or regular-grid configuration, which means the center-boundary configuration can save a large amount of sensors and signal processing resources for engineering applications.

In summary, the optimization method is effective to search for proper sensor configurations. The center-boundary configuration found by the optimization method is different from traditional ones and has obvious advantage of inversion accuracy over traditional ones.

5. Discussion

Based on the optimization method proposed in Section 3, we studied the parameters of region shapes, sensor numbers and source deviation, and analyzed the effect of those factors on the moment tensor inversion. The discussion part attempt to provide some general guidelines of sensor arrangement for the engineering applications of the moment tensor inversion.

5.1. Region shape

For the synthetic tests in Section 4, the feasible region, in which sensors can be deployed, is circular. In this section, we changed the circular region to some other shapes and studied the sensor configurations in those regions. As shown in Section 4, the sensor configurations of different sensor numbers are similar to each other, thus 6 sensors are used for the study. Based on the optimization method, the best sensor configurations for four regions are plotted in Fig. 10 and the region shapes are triangle, square, pentagon and hexagon respectively.

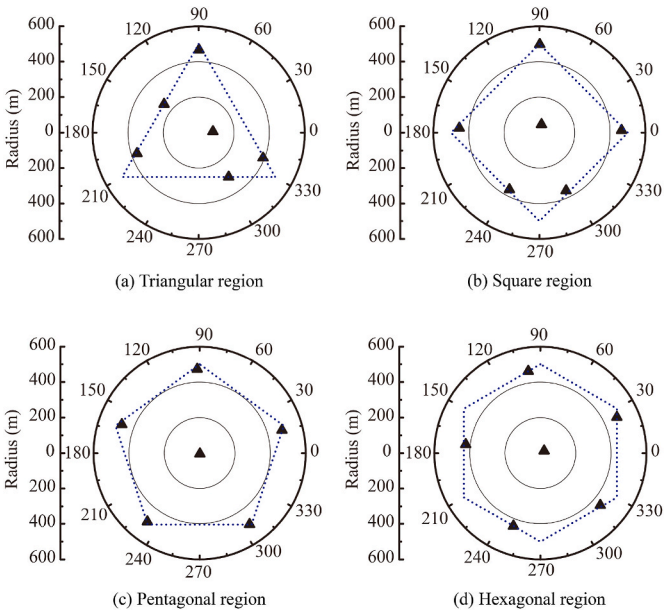

Fig. 10. Optimized sensor configurations for (a) triangular, (b) square, (c) pentagonal and (d) hexagonal regions.

Table 2
Condition numbers for 5 shapes of regions.

Shape	Triangle	Square	Pentagon	Hexagon	Circular
Condition number	23.27	17.69	12.11	13.75	12.11

As shown in Fig. 10, the sensor configurations for different region shapes still have the center-boundary character, which one sensor locates at the center and the others locate around. However, for the shapes of triangular and square, the included angles between sensors are limited by the boundaries and different for different sensors. The condition numbers for the four sensor configurations are listed in Table 2.

As listed in Table 2, the condition numbers for the triangular and square regions are relatively larger than those for pentagonal, hexagonal and circular regions. Obviously, the condition number for the pentagonal region is the same as that for circular regions. For the moment tensor inversion, at least 6 sensors of single channel are required for one

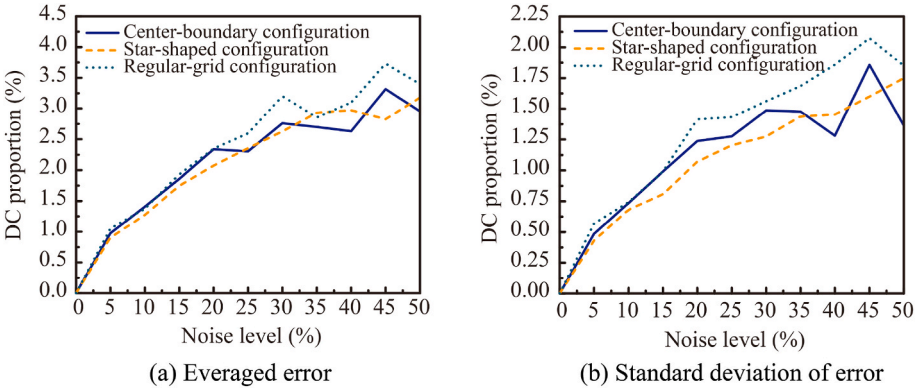

Fig. 9. Inversion errors of the three sensor configurations: center-boundary configuration of 19 sensors, star-shaped configuration of 73 sensors and regular-grid configuration of 81 sensors.

source. For the 6 sensors arranged as the center-boundary configuration, 5 sensors are on the boundary of the region. Thus 5 edges of the region are required to locate the sensors. For mores sensors, more than 5 sensors are arranged on the boundary, thus a circular region is better for sensor arrangements than polygon regions.

5.2. Sensor number

The number of sensors needed in the inversion is a key problem, which determines the complexity and resource consumption of the moment tensor inversion for engineering applications. In this section, we studied the sensor numbers for different sizes of feasible regions and the performance of sensor configurations is indicated by condition numbers. According to the theoretical analysis in Section 2.2, the smaller the condition number is, the better the performance of sensor configurations. The feasible region is circular and sensors are arranged as the center-boundary configurations.

It is generally believed that more sensors are helpful for improving the inversion accuracy for moment tensors. However, this guideline is imperfect for some conditions and needs further explanation. For the center-boundary configuration, the relationship between sensor numbers and condition numbers is plotted in Fig. 11. Various sizes of feasible regions are involved in this section and defined as the ratios between the radii of feasible regions and the depth of sources (R/H). Lines types in Fig. 11 represent the results for different ratios.

As shown in Fig. 11, more sensors are helpful for improving inversion accuracy, but there are limits to the improvement. As the increase of sensor numbers, condition numbers decrease and approach specific values. Specifically, the decreasing speed and specific values are dependent on the sizes of feasible region. For small regions, the sensor numbers for reaching the minimum condition numbers are small, but the minimum condition numbers are relatively large. For large regions, more sensors are needed to achieve the minimum condition numbers, but the condition numbers are relatively small. In summary, for improving the inversion accuracy, large feasible regions are recommended for the moment tensor inversion and more sensors are needed to achieve the minimum condition numbers.

5.3. Source deviation

The optimization of sensor configurations is based on the prediction of source locations. If sources deviate from the predicted locations, the best sensor configuration and condition numbers will change.

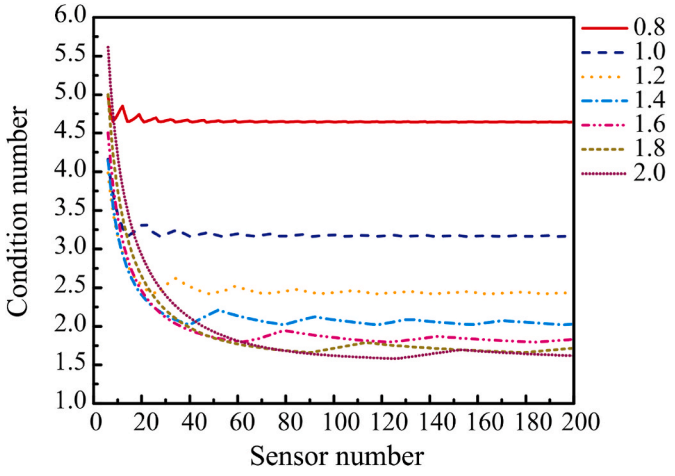

Fig. 11. Condition numbers for various sensor numbers. Small condition numbers represent high performance of sensor configurations. Line types represent the ratios between the radii of feasible regions and the depth of sources (R/H). Sensors are arranged as the center-boundary configuration with one sensor at the center and multiple sensors around.

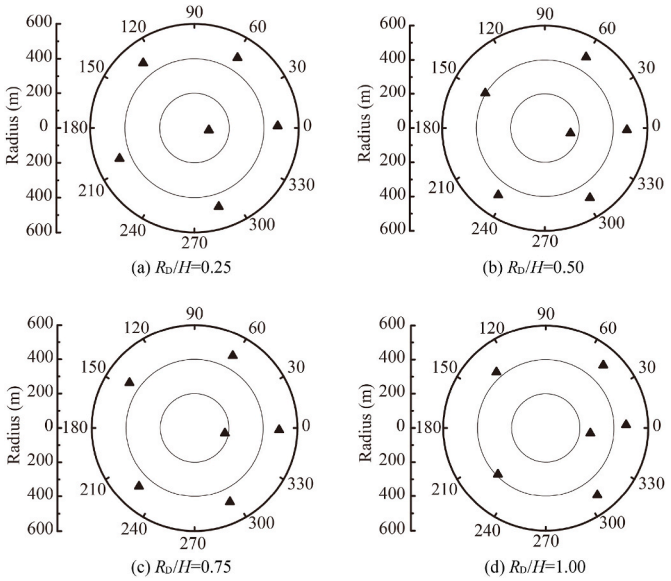

Fig. 12. Sensor configurations for different source deviations. R_D are the source deviations and H is the depth of sources.

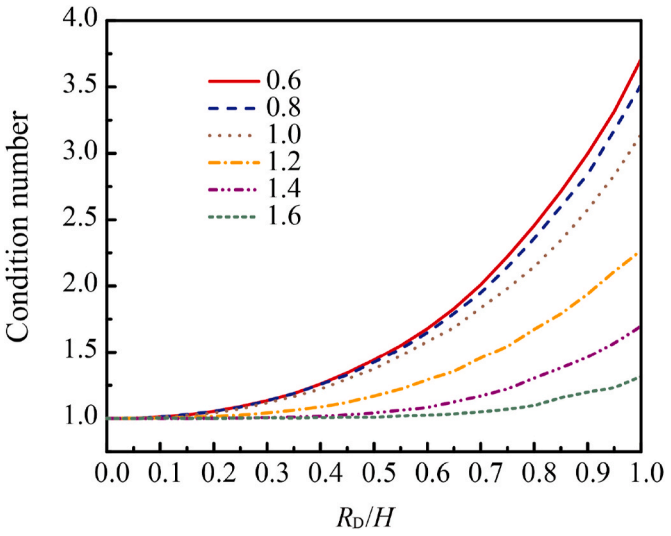

Fig. 13. Condition numbers for different source deviations. R_D are the source deviations, H is the depth of sources. Line types represent the results for different sizes of feasible regions and labeled as R/H, which R are the radii of the feasible regions. For each line type, the condition numbers are normalized by that for $R_D/H = 0$.

In this section, we studied the effect of deviations of sources on sensor configurations. For the synthetic tests in Section 4, the sources are directly below the feasible regions. In this section, the depth H of sources remains unchanged and the deviations R_D are defined as the distance along the 0-degree direction from the expected to real positions. The sensor configurations of 6 sensors are studied for different source deviations by the optimization method. The sensor configurations for various deviations R_D/H are plotted in Fig. 12.

As shown in Fig. 12, when sources are no longer directly below the feasible region, the sensor configurations will change. The center sensor moves in the deviation direction of the source. The deviation of the center sensor increases with the increase of source deviations. For different source deviations, the condition numbers are plotted in Fig. 13.

As shown in Fig. 13, condition numbers increase with the increase of

source deviations, which means that source deviations are harmful to inversion accuracy. The effect of source deviations on condition numbers is dependent on the sizes of feasible regions. For large regions, the condition numbers for specific source deviations are relatively small. In summary, If the source locations can not be accurately predicted, larger regions for sensor arrangement are recommended.

6. Conclusion

For the moment tensor inversion, sensor configurations have significant influence on inversion accuracy. In this paper, we analyzed the mechanism of sensor arrangements to suppress the effect of noise mathematically and provided an optimization method to search for proper sensor configurations for engineering applications. For evaluating the optimization method, synthetic P waves contaminated by random white noise with a uniform distribution are used to test the optimized sensor configurations, and the effectiveness and efficiency of the optimization method is validated. Based on this optimization method, we studied the sensor configurations for some general conditions.

The conclusions are arrived as follows:

(1) By the optimized sensor configurations, inversion errors can be equally distributed among moment-tensor elements to improve the accuracy of source-type interpretation.
(2) For surface arrays, the sensor configurations, in which one or more sensors locate at the center and the others locate around, are recommended for the moment tensor inversion.
(3) There are upper limits to the numbers of sensors for specific engineering applications and more sensors are not helpful for improving inversion accuracy.
(4) For improving inversion accuracy, large and circular regions for sensor arrangements are recommended.

Credit author statement

Yue Kong: Conceptualization; Data curation; Investigation; Validation; Writing – original draft. **Weimin Chen**: Data curation; Funding acquisition; Methodology; Project administration; Supervision. **Ning Liu**: Funding acquisition; Investigation; Validation. **Boqi Kang**: Formal analysis; Validation. **Min Li**: Conceptualization; Formal analysis; Methodology; Project administration; Supervision.

Declaration of competing interest

The authors declare that they have no known competing financial interests or personal relationships that could have appeared to influence the work reported in this paper.

Acknowledgements

The authors of this paper would like to thank the financial supports provided by the Strategic Priority Research Program of the Chinese Academy of Sciences (Grant No. XDA22000000) and National Natural Science Foundation of China (Grant No. 41804134).

References

Aki, K., Richards, P.G., 2002. Quantitative Seismology. University Science Books, Sausalito, CA.
Baig, A., Urbancic, T., 2010. Microseismic moment tensors: a path to understanding frac growth. Lead. Edge 29 (3), 320–324.
Battiti, R., 1992. First- and second-order methods for learning: between steepest descent and Newton's method. Neural Comput. 4 (2), 141–166.
Burridge, R., Knopoff, L., 1964. Body force equivalents for seismic dislocations. Bull. Seismol. Soc. Am. 54 (6A), 1875–1888.
Davi, R., Vavryčuk, V., Charalampidou, E.-M., Kwiatek, G., 2013. Network sensor calibration for retrieving accurate moment tensors of acoustic emissions. Int. J. Rock Mech. Min. 62, 59–67.
Dufumier, H., Rivera, L., 1997. On the resolution of the isotropic component in moment tensor inversion. Geophys. J. Int. 131 (3), 595–606.
Duncan, P.M., Eisner, L., 2010. Reservoir characterization using surface microseismic monitoring. Geophysics 75 (5), A139–A146.
Dziewonski, A., Chou, T.A., Woodhouse, J.H., 1981. Determination of earthquake source parameters from waveform data for studies of global and regional seismicity. J. Geophys. Res. Solid Earth 86 (B4), 2825–2852.
Eyre, T.S., Van Der Baan, M., 2017. The reliability of microseismic moment-tensor solutions: surface versus borehole monitoring. Geophysics 82 (6), KS113–KS125.
Eyre, T.S., Van Der Baan, M., 2015. Overview of moment-tensor inversion of microseismic events. Lead. Edge 34 (8), 882–888.
Fischer, T., Guest, A., 2011. Shear and tensile earthquakes caused by fluid injection. Geophys. Res. Lett. 38 (5), L05307.
Fojtíková, L., Vavryčuk, V., Cipciar, A., Madarás, J., 2010. Focal mechanisms of micro-earthquakes in the dobrá voda seismoactive area in the malé karpaty mts. (little carpathians), Slovakia. Tectonophysics 492 (1–4), 213–229.
Godano, M., Bardainne, T., Regnier, M., Deschamps, A., 2011. Moment-tensor determination by nonlinear inversion of amplitudes. Bull. Seismol. Soc. Am. 101 (1), 366–378.
Grosse, C.U., Ohtsu, M., 2008. Acoustic Emission Testing. Springer Berlin Heidelberg.
Hampton, J., Gutierrez, M., Matzar, L., 2019. Microcrack damage observations near coalesced fractures using acoustic emission. Rock Mech. Rock Eng. 52 (10), 3597–3608.
Hardebeck, J.L., Shearer, P.M., 2003. Using S/P amplitude ratios to constrain the focal mechanisms of small earthquakes. Bull. Seismol. Soc. Am. 93 (6), 2434–2444.
Hossain, M., Rahman, M., Rahman, S., 2000. Hydraulic fracture initiation and propagation: roles of wellbore trajectory, perforation and stress regimes. J. Pet. Sci. Eng. 27 (3–4), 129–149.
Hudson, J.A., Pearce, R.G., Rogers, R.M., 1989. Source type plot for inversion of the moment tensor. J. Geophys. Res. 94, 765–774.
Hughes, J.D., 2013. A reality check on the shale revolution. Nature 494 (7437), 307–308.
Jechumtalova, Z., Eisner, L., 2008. Seismic source mechanism inversion from a linear array of receivers reveals non-double-couple seismic events induced by hydraulic fracturing in sedimentary formation. Tectonophysics 460 (1–4), 124–133.
Jechumtálová, Z., Šílený, J., 2005. Amplitude ratios for complete moment tensor retrieval. Geophys. Res. Lett. 32 (22), L22303.
Jian, P.R., Tseng, T.L., Liang, W.T., Huang, P.H., 2018. A new automatic full-waveform regional moment tensor inversion algorithm and its applications in the Taiwan area. Bull. Seismol. Soc. Am. 108 (2), 573–587.
Kikuchi, M., Kanamori, H., 1991. Inversion of complex body waves—III. Bull. Seismol. Soc. Am. 81 (6), 2335–2350.
Kong, Y., Li, M., Chen, W.M., 2019. Sensor arrangement in moment-tensor inversion for cracks. J. Beijing Univ. Aeronaut. Astronaut. 45 (7), 1380–1387 (in Chinese).
Kwiatek, G., Charalampidou, E.-M., Dresen, G., Stanchits, S., 2014. An improved method for seismic moment tensor inversion of acoustic emissions through assessment of sensor coupling and sensitivity to incidence angle. Int. J. Rock Mech. Min. 65, 153–161.
Li, L., et al., 2019. A review of the current status of induced seismicity monitoring for hydraulic fracturing in unconventional tight oil and gas reservoirs. Fuel 242, 195–210.
Liu, P.X., Chen, S.Y., Guo, Y.S., Li, P.C., 2014. Moment tensor inversion of acoustic emission. Chin. J. Geophys. 57 (3), 858–866 (in Chinese).
Loke, M.H., Barker, R.D., 1996. Rapid least-squares inversion of apparent resistivity pseudosections by a quasi-Newton method1. Geophys. Prospect. 44 (1), 131–152.
Miller, A.D., Julian, B.R., Foulger, G.R., 1998. Three-dimensional seismic structure and moment tensors of non-double-couple earthquakes at the Hengill–Grensdalur volcanic complex, Iceland. Geophys. J. Int. 133 (2), 309–325.
Napoli, V.J., Ebel, J.E., 2018. Relative location analysis and moment tensor inversion of the 2012 Gulf of Maine earthquake swarm. Seismol Res. Lett. 89 (1), 229–240.
Ohtsu, M., 1988. Source inversion of acoustic emission waveform. Dob. Gakkai Ronbunshu 1988 (398), 71–79.
Ohtsu, M., 1991. Simplified moment tensor analysis and unified decomposition of acoustic emission source: application to in situ hydrofracturing test. J. Geophys. Res. Solid Earth 96 (B4), 6211–6221.
Petruzalek, M., et al., 2018. Acoustic emission in a laboratory: mechanism of microearthquakes using alternative source models. J. Geophys. Res. Solid Earth 123 (6), 4965–4982.
Ren, Y., Gao, Y., Wu, S., Vavryčuk, V., 2020. Optimum size and density of surface grid arrays for retrieving accurate shear-tensile fracturing of microearthquakes. Geophys. Prospect. 68 (8), 2347–2360.
Savard, G., Gauvin, J., 1994. The steepest descent direction for the nonlinear bilevel programming problem. Oper. Res. Lett. 15 (5), 265–272.
Shearer, P.M., 2009. Introduction to Seismology. Cambridge University Press.
Silený, J., 2009. Resolution of non-double-couple mechanisms; simulation of hypocenter mislocation and velocity structure mismodeling. Bull. Seismol. Soc. Am. 99 (4), 2265–2272.
Šílený, J., Panza, G.F., Campus, P., 1992. Waveform inversion for point source moment tensor retrieval with variable hypocentral depth and structural model. Geophys. J. Int. 109 (2), 259–274.
Sipkin, S.A., 1982. Estimation of earthquake source parameters by the inversion of waveform data: synthetic waveforms. Phys. Earth Planet. In. 30 (2–3), 242–259.
Soeder, D.J., 2018. The successful development of gas and oil resources from shales in North America. J. Pet. Sci. Eng. 163, 399–420.

Spikin, S.A., 1986. Estimation of earthquake source parameters by the inversion of waveform data: global seismicity, 1981-1983. Bull. Seismol. Soc. Am. 76 (6), 1515–1541.
Stanek, F., Eisner, L., Moser, T.J., 2014. Stability of source mechanisms inverted from P-wave amplitude microseismic monitoring data acquired at the surface. Geophys. Prospect. 62 (3), 475–490.
Stierle, E., Vavryčuk, V., Kwiatek, G., Charalampidou, E.M., Bohnhoff, M., 2016. Seismic moment tensors of acoustic emissions recorded during laboratory rock deformation experiments: sensitivity to attenuation and anisotropy. Geophys. J. Int. 205 (1), 38–50.
Takemura, S., Kimura, T., Saito, T., Kubo, H., Shiomi, K., 2018. Moment tensor inversion of the 2016 southeast offshore Mie earthquake in the Tonankai region using a three-dimensional velocity structure model: effects of the accretionary prism and subducting oceanic plate. Earth Planets Space 70, 19.
Tape, W., Tape, C., 2012. A geometric comparison of source-type plots for moment tensors. Geophys. J. Int. 190 (1), 499–510.
Vavryčuk, V., 2007. On the retrieval of moment tensors from borehole data. Geophys. Prospect. 55 (3), 381–391.
Vavryčuk, V., 2011. Tensile earthquakes: theory, modeling, and inversion. J. Geophys. Res. Solid Earth 116 (B12).
Vavryčuk, V., 2015. Moment tensor decompositions revisited. J. Seismol. 19 (1), 231–252.
Vavryčuk, V., Adamova, P., Doubravova, J., Jakoubkova, H., 2017. Moment tensor inversion based on the principal component analysis of waveforms: method and application to microearthquakes in West Bohemia, Czech Republic. Seismol Res. Lett. 88 (5), 1303–1315.
Vavryčuk, V., Bohnhoff, M., Jechumtálová, Z., Kolář, P., Šílený, J., 2008. Non-double-couple mechanisms of microearthquakes induced during the 2000 injection experiment at the KTB site, Germany: a result of tensile faulting or anisotropy of a rock? Tectonophysics 456 (1–2), 74–93.
Wu, S., et al., 2019. Shear-tensile fractures in hydraulic fracturing network of layered shale. J. Pet. Sci. Eng. 183, 12.
Xing, Z.D., Cao, J.R., 2005. Matrix Numerical Analysis. Shaanxi Science and Technology Press, Shaanxi (in Chinese).
Xu, S.D., Li, Y.H., Liu, J.P., 2017. Detection of cracking and damage mechanisms in brittle granites by moment tensor analysis of acoustic emission signals. Acoust Phys. 63 (3), 359–367.
Yu, C., Vavryčuk, V., Adamová, P., Bohnhoff, M., 2018. Moment tensors of induced microearthquakes in the Geysers Geothermal reservoir from broadband seismic recordings: implications for faulting regime, stress tensor, and fluid pressure. J. Geophys. Res. Solid Earth 123 (10), 8748–8766.
Yu, H.Z., Zhu, Q.Y., Yin, X.C., Wang, Y.C., 2005. Moment tensor analysis of the acoustic emission source in the rock damage process. Prog. Nat. Sci. 15 (7), 609–613.
Zhang, Q., et al., 2020. Study of interaction mechanisms between hydraulic fracture and weak plane with different strengths and widths using the bonded-particle model based on moment tensors. Eng. Fract. Mech. 225, 106813.
Zhuang, L., Zang, A., 2021. Laboratory hydraulic fracturing experiments on crystalline rock for geothermal purposes. Earth Sci. Rev. 216.